

Molecular Gas Properties in M83 from CO PDFs

FUMI EGUSA,^{1,2} AKIHIKO HIROTA,^{2,3} JUNICHI BABA,^{4,5} AND KAZUYUKI MURAOKA⁶

¹*Institute of Space and Astronautical Science, Japan Aerospace Exploration Agency, Sagamihara, Kanagawa, Japan*

²*Chile Observatory, National Astronomical Observatory of Japan, Mitaka, Tokyo, Japan*

³*Joint ALMA Observatory, Santiago, Region Metropolitana, Chile*

⁴*Research Center for Space and Cosmic Evolution, Ehime University, Matsuyama, Ehime, Japan*

⁵*National Astronomical Observatory of Japan, Mitaka, Tokyo, Japan*

⁶*Department of Physical Science, Osaka Prefecture University, Sakai, Osaka, Japan*

ABSTRACT

We have obtained ¹²CO(1–0) data of the nearby barred spiral galaxy M83 from Atacama Large Millimeter/submillimeter Array and Nobeyama 45m observations. By combining these two data sets, the total CO flux has been recovered, and a high angular resolution (2'' corresponding to ~ 40 pc at the distance of M83) has been achieved. The field of view is 3' corresponding to ~ 3.4 kpc and covers the galactic center, bar, and spiral arm regions. In order to investigate how these galactic structures affect gas properties, we have created a probability distribution function (PDF) of the CO integrated intensity (I_{CO}), peak temperature, and velocity dispersion for a region with each structure. We find that the I_{CO} PDF for the bar shows a bright-end tail while that for the arm does not. Since the star formation efficiency is lower in the bar, this difference in PDF shape is contrary to the trend in Milky Way studies where the bright-end tail is found for star-forming molecular clouds. While the peak temperature PDFs are similar for bar and arm regions, velocity dispersion in bar is systematically larger than in arm. This large velocity dispersion is likely a major cause of the bright-end tail and of suppressed star formation. We also investigate an effect of stellar feedback to PDF profiles and find that the different I_{CO} PDFs between bar and arm regions cannot be explained by the feedback effect, at least at the current spatial scale.

Keywords: galaxies: individual (M83 or NGC 5236) – galaxies: structure – ISM: molecules

1. INTRODUCTION

The evolution of interstellar medium (ISM) in galactic disks is intimately related to star formation and galaxy evolution. In external face-on galaxies, compared to Milky Way (MW), it is easier to investigate ISM conditions and their evolution while rotating in the disk. Recent observations have reported that ISM conditions depend on associated galactic structures, such as spiral arms and bars. For example, massive clouds tend to reside in spiral arms (Koda et al. 2009; Colombo et al. 2014), suggesting that spiral arms play an important role to form massive clouds that are plausible precursors of massive star clusters. Line ratios have also been found to be different among disk structures (e.g. Koda et al. 2012; Tosaki et al. 2017), representing dif-

ferent physical conditions. High resolution observations revealed ISM evolution within spiral arms (Egusa et al. 2011; Hirota et al. 2011), clouds at the downstream side of spiral arms being more massive and star-forming. In bar regions, molecular gas is concentrated in ridges and bar edges (e.g. Sheth et al. 2002) but star formation efficiency is relatively low especially in ridges (e.g. Momose et al. 2010; Sorai et al. 2012; Pan & Kuno 2017). Recent numerical calculations have also suggested that ISM conditions depend on dynamical environments (e.g. Fujimoto et al. 2014b; Nguyen et al. 2017).

Many of studies mentioned above defined clouds using cloud identifying algorithms. One caveat of such algorithms is that they tend to identify structures whose size is similar to an angular resolution. As a result, a dynamic range of cloud size is rather small. In addition, recent numerical simulations suggest that molecular clouds are not isolated and discrete structures but

are part of continuous fluid (e.g. Dobbs & Pringle 2013). For example, Colombo et al. (2014) identified > 1500 clouds in the nearby spiral galaxy M51 from a CO(1–0) data set at 40 pc resolution and most of the clouds have a radius between 20 pc and 100 pc (i.e. the dynamic range is ~ 1 dex, their Figure 8). They also calculated the mass in the clouds to be about half of the total mass. The cloud analysis cannot take into account such gas outside identified clouds whose mass can be comparable to that inside the clouds.

Another and complementary way of measuring ISM properties is to use a probability distribution function (PDF), which is a normalized histogram of a physical parameter or an observed quantity. Advantages of PDF analysis are that it is free of any biases due to cloud identification and that it includes ISM components which would not be included in identified clouds.

For Milky Way (MW) molecular clouds, the PDF of gas column density has been used to investigate their star-forming conditions. Kainulainen et al. (2009) created gas column density PDFs based on NIR extinction maps and found that those for star-forming clouds show a power-law (PL) like tail while those for quiescent clouds show a log-normal (LN) profile. Such different PDF profiles have been interpreted as different ISM conditions – LN for turbulence-dominated clouds (e.g. Nordlund & Padoan 1999) and PL for self-gravity-dominated clouds (e.g. Kritsuk et al. 2011; Girichidis et al. 2014) or clouds with high density contrast (Elmegreen 2011). Brunt (2015) claimed that the tail can be explained as a part of a wide LN profile which corresponds to a cold gas component.

Brightness distribution function (BDF) introduced by Sawada et al. (2012b) is a PDF of CO brightness temperature. Together with their following study (Sawada et al. 2012a), they found that BDFs for spiral arms in MW tend to show a bright-end tail compared to interarm regions. Meanwhile, Rathborne et al. (2014) presented that a cloud close to the MW center shows a PDF peaking at a higher density compared to clouds in the solar neighborhood. The PDF peak corresponds to a mean density and the authors attributed this difference to high-pressure environments around the MW center.

For external galaxies, Hughes et al. (2013) created PDFs for galactic structures of M51 from CO(1–0) data at ~ 40 pc scale and found different PDF shapes among the structures. The difference is more clearly seen in PDFs of the integrated CO intensity in the sense that center and arm PDFs are wider and deviate from LN profiles while interarm PDFs are narrower and close to LN profiles. Interestingly, PDFs for the center and arm

where star formation is relatively active appear to be truncated rather than extended. They interpreted this truncation as a feedback effect. They also claimed that the narrow LN profiles in the interarm are a sign of turbulence dominated ISM. Druard et al. (2014) created a PDF at ~ 50 pc scale for M33 based on CO(2–1) integrated intensity and found that its shape positively deviates from the LN profile at $N(\text{H}_2) > 2 \times 10^{21} \text{ H}_2/\text{cm}^2$. They attributed this bright-end excess to self-gravity, although the threshold column density is low (comparable to the nominal 3σ limit of M51 data by Hughes et al. (2013)). We should note here that spatial resolutions of these studies are much larger than those of MW studies. Thus, a direct comparison of MW and these studies is not straightforward.

Hughes et al. (2013) also investigated how data quality (i.e. resolution and sensitivity) and technique to create integrated intensity maps affect PDF shapes. Their results suggest that the high spatial resolution is important to investigate bright-end profiles. The importance of spatial resolution is also pointed out by numerical simulations in Wada & Norman (2007). Consistently, Berkhuijsen & Fletcher (2015) found that PDFs of gas surface densities for M31 and M51 at ~ 300 pc scale are well fitted by LN profiles. Ossenkopf-Okada et al. (2016) investigated how observing conditions affect PDF shapes. In particular, they presented that interferometric observations should distort overall PDF shapes, i.e. their faint-end profile, peak position, and bright-end profile. To minimize the distortion, a dense uv sampling especially at low spatial frequencies is necessary. Given this dependency, we compare PDF profiles only within a galaxy and do not directly compare the results with other galaxies.

In this paper, we present CO PDFs for the nearby ($D = 4.5$ Mpc; Thim et al. 2003) face-on (inclination angle = 24° ; Comte 1981) barred spiral (SAB(s)c; de Vaucouleurs et al. 1991) galaxy M83 (or NGC 5236). Its proximity and disk orientation are well suited to study ISM properties and their relationship to disk structures. We find that PDFs differ significantly among the galactic structures and discuss the origin of this difference. Stellar feedback effects on PDF profiles are also investigated. This is a complementary study to Hirota et al. (submitted, hereafter paper I), which investigates cloud properties based on the same data set.

2. OBSERVATIONS AND DATA REDUCTION

The rotational transitions of CO are the most widely used tracers of molecular gas, and their integrated intensities have been used to estimate the column density of molecular hydrogen (e.g. Young & Scoville 1991;

Bolatto et al. 2013). We have mapped a central disk area of M83 in the $^{12}\text{CO}(1-0)$ emission using Atacama Large Millimeter/submillimeter Array (ALMA) and the Nobeyama 45m telescope (NRO45m). A detail of observations and data reduction will be in paper I, and we provide a summary here.

2.1. ALMA observations

The data have been obtained for the Cycle 0 project 2011.0.00772.S, and consist of two Execution Blocks (EBs) with a compact configuration and three EBs with an extended configuration. The field of view (FoV) is about $2.6' \times 2.6'$ with 45 mosaic pointings, which includes the galactic center, a northern part of the bar, and a spiral arm.

2.2. Nobeyama 45m observations

The NRO45m observations were carried out using the on-the-fly mode with the T100 receiver and SAM45 spectrometers. The entire FoV includes the ALMA FoV.

2.3. Data combination

In order to combine the ALMA and NRO45m data, the NRO45m map is first converted to a uv data set. Then, the two uv data sets from ALMA and NRO45m are Fourier-transformed and deconvolved together.

The synthesized beam is $2.0'' \times 1.1''$ in full width at half maximum. At the distance of M83, this corresponds to $45 \text{ pc} \times 24 \text{ pc}$. We adopt a 1σ sensitivity of each channel to be 8.0 mJy/beam or 0.33 K with a channel width of 2.6 km/s. The pixel size is set to be $0.25''$.

The moment 0 (i.e. integrated intensity; I_{CO}) and moment 2 (i.e. velocity dispersion; σ_V) maps are created by applying the mask that includes all the pixels with $S/N \geq 4$ and those with $S/N \geq 2$ and morphologically connected to the former pixels. The noise map is not uniform according to the primary beam pattern and to different observing conditions (e.g. integration time) between mosaic pointings. A typical 1σ sensitivity of the integrated intensity map is estimated to be 47 mJy/beam km/s or 1.8 K km/s. Assuming the Galactic conversion factor, $X_{\text{CO}} = 2 \times 10^{20} \text{ H}_2/\text{cm}^2/(\text{K km/s})$ (Dame et al. 2001), this sensitivity corresponds to $\Sigma = 3.6 \times 10^{20} \text{ H}_2/\text{cm}^2$ or $5.8 M_{\odot}/\text{pc}^2$. Note that this is not corrected for inclination.

3. CO PDFS

In this section, we present PDFs of the integrated intensity (I_{CO}), the peak temperature (T_{peak}), and the velocity dispersion (σ_V), and discuss their profiles according to disk structures (§3.1) and to stellar feedback (§3.2). Note that σ_V is not corrected for the galactic rotation and beam smearing. As described in Appendix,

these effects do not affect the following results and discussions.

3.1. Disk structures

According to the Fourier analysis of K_s -band image by Hirota et al. (2014, hereafter H14), we define the radial range of the bar to be $r = 20''-85''$. This is the region where non-circular motions are clearly seen in a position-velocity diagram (their Figure 7). The semi-minor axis of the bar is set to be $46''$ based on an ellipse fitting to the same K_s -band image. A region outside the bar, mostly consists of a spiral arm, is called an arm region. A region inside the bar is called a center region. The center and bar regions are indicated by dots-dashed and dashed lines in Figure 1 (left), respectively. The definition in this paper is different and more simple compared to that of paper I, for the sake of better statistics especially for PDF profiles at the bright end.

3.1.1. I_{CO} PDF

The I_{CO} map and its PDF for each of the three regions are presented in Figure 1. Peak positions of bar and arm PDFs are similar (10–30 K km/s), while that for center is an order of magnitude higher. This difference in peak position is similar to what is found for MW clouds (Rathborne et al. 2014). We have confirmed that this general trend holds when the outer boundary of the center region is changed to $r = 10''$ or $30''$.

The arm PDF is likely LN or at least without a clear PL tail. Its shape as well as the dynamic range of gas surface density are similar to those of spiral arms in M51 derived by Hughes et al. (2013). In the rightmost panel of Figure 1, an LN function fitted to the arm PDF above 3σ (the gray dot-dashed vertical line) is presented by the black dotted line. The arm PDF appears to be slightly truncated at the bright end, but the fit result highly depends on the range used for the fit. Furthermore, as already mentioned in §1, Ossenkopf-Okada et al. (2016) presented that PDF profiles are highly sensitive to the data quality – not only the sensitivity but also the uv coverage. In this study, we thus use this LN profile only for the purpose of guiding the eye, and do not compare the shape of profiles with other studies.

On the other hand, PDFs for the center and bar regions extend to higher densities compared to the arm PDF. The center PDF appears to have two peaks, while the bar PDF exhibits a PL like tail at the bright end ($I_{\text{CO}} \gtrsim 100 \text{ K km/s}$). The excess is also clear when compared to the LN profile (Figure 1 (right)). As seen in Figure 1 (left), such bright emission comes from the molecular ridges close to the center region and not so much gas concentration is found in the northern bar end. This is consistent with previous CO observations

of M83, where gas concentration is found only at the southern bar end (H14), which is not covered by the current FoV.

From PDF studies of MW clouds, a column density PDF with a bright-end tail has been regarded as a sign of star formation (Kainulainen et al. 2009). However, star formation efficiency (SFE = star formation rate / (molecular) gas mass) in the bar of M83 is lower than that in the arms (H14). One reason for this difference would be the difference in spatial scales. While MW studies discuss PDF profiles at pc scale within a cloud, M83 PDFs in this paper are at 40 pc scale, which is comparable to a typical MW cloud size. Results presented here indicate that at this scale, an existence of a bright-end tail of an I_{CO} PDF is not always the sign of active star formation. In the following subsections, we further discuss possible explanations for this finding.

3.1.2. T_{peak} and σ_V PDF

In order to investigate the reason for the difference in I_{CO} PDFs between the bar and arm regions, we create PDFs of other observed properties. Figure 2 presents the T_{peak} map and its PDFs, while Figure 3 presents those for σ_V . While T_{peak} PDFs do not differ between the bar and arm regions, the σ_V PDF for the bar is shifted to the right-hand side of that for the arm. In M51, Hughes et al. (2013) found a similar trend that their brightness temperature PDFs are more similar between structures compared to I_{CO} PDFs. Since $I_{\text{CO}} \sim T_{\text{peak}} \times \sigma_V$, this large velocity dispersion in the bar region likely results in the bright-end tail of the I_{CO} PDF. A reason for this large velocity dispersion would be one or combination of large shear motions within the bar, large random motions within a cloud, and overlaps or collisions of clouds at different velocities. The second point is supported by large velocity dispersions of molecular clouds in the bar presented in paper I. A more detailed discussion on how these dynamic properties of molecular gas are related to star formation activities is given in §4.

For the center region, both T_{peak} and σ_V show different PDF profiles compared to the other regions. The excess in the I_{CO} PDF comes from both high T_{peak} and large σ_V . Such high T_{peak} and large σ_V are also observed in individual clouds identified in paper I. The high T_{peak} is a sign of high gas temperature due to the circumnuclear starburst (e.g. Knapen et al. 2010; Wofford et al. 2011) and/or a large filling factor. The large σ_V comes from either large streaming motions or highly turbulent clouds.

3.2. Stellar feedback

Another explanation for the different I_{CO} PDFs is that the arm PDF is truncated due to the effect of stellar feedback such as radiation pressure, photoionization, and supernova explosion (Hopkins et al. 2012). Such stellar feedback mechanisms can preferentially destroy dense gas around young stars, and thus truncate density PDFs at the bright end.

In order to investigate the feedback effect on PDF profiles, we have defined “feedback area” to be within 2'' from known young star clusters, HII regions, or supernova remnants (SNRs), where stronger feedback is expected. The catalogs we use in this paper are Whitmore et al. (2011) for young star clusters (their categories 3, 4a, and 4b only), H14 for bright HII regions (sources with $L(\text{H}\alpha) > 10^{37.6}$ erg/s only), and Dopita et al. (2010) and Blair et al. (2012, 2014) for SNR candidates. We have confirmed that > 90% of sources within our FoV have radius < 2''. The defined feedback area are indicated by circles in the left panel of Figure 4.

3.2.1. I_{CO} PDF

PDFs for feedback and non-feedback area are presented in the right panel of Figure 4. Since we are interested in difference between bar and arm regions, the center region (enclosed by a dots-dashed line in the left panel of Figure 4) is excluded. Contrary to the theoretical expectation, the bright-end slopes of these two PDFs are not significantly different. Based on numerical simulations by Hopkins et al. (2012), we fit each PDF at $\Sigma > 10^3 M_{\odot}/\text{pc}^2 = 6 \times 10^{22} \text{ H}_2/\text{cm}^2$ with a line. The fit is performed in the log-log space using the least chi-square method. Although the number of data points that exceed this gas density limit is small, slopes of the two fitted lines (solid cyan lines in Figure 4) are consistent within errors. We thus deduce that at least at this spatial scale (i.e., ~ 40 pc in radius) the feedback effect is not dominant in shaping the bright-end profiles of I_{CO} PDFs.

We have also tried different definition of radius ($r = 1''$ and $3''$) for the feedback area. For the former case, the bright-end slope is steeper for the feedback area than that for the non-feedback area. However, the feedback PDF has only two data points above the threshold, which results in failure of deriving errors. For the latter case, the slope is shallower for the feedback area than that for the non-feedback area. A naive interpretation of this result is that stellar feedback reduces the amount of dense gas within 20 pc and increases it at 60 pc away from the source. The former is consistent with the general understanding that stellar feedback effect should be larger when closer to the source. The latter may indicate

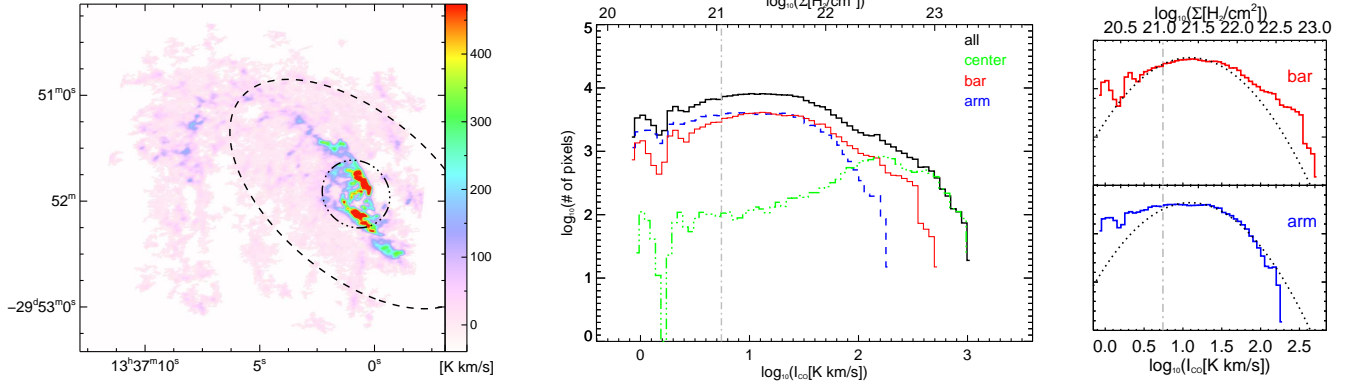


Figure 1. *Left:* The I_{CO} map of M83 from ALMA+NRO45m observations. The coordinates are Right Ascension and Declination in ICRS. The outer boundary of center and bar regions are indicated by 3dots-dashed and dashed lines, respectively. *Middle:* The I_{CO} PDFs for the center (green 3dots-dashed), bar (red solid), and arm (blue dashed) regions. The black solid line is the PDF for the entire FoV. The vertical gray dot-dashed line indicates the 3σ of I_{CO} . The horizontal axis on top is the molecular gas surface density in H_2/cm^2 , calculated assuming the Galactic conversion factor. *Right:* The same I_{CO} PDFs for the bar and arm with an LN function (black dotted line).

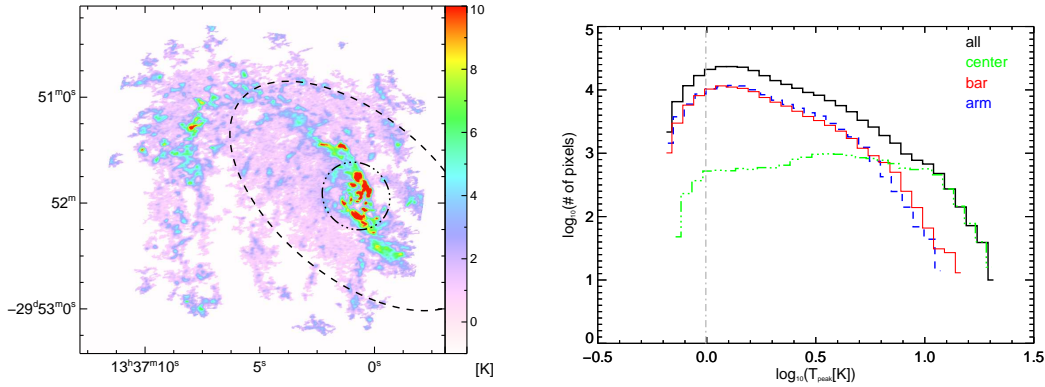


Figure 2. Same as Figure 1, but for T_{peak} . The vertical gray dot-dashed line indicates the 3σ of channel maps in K.

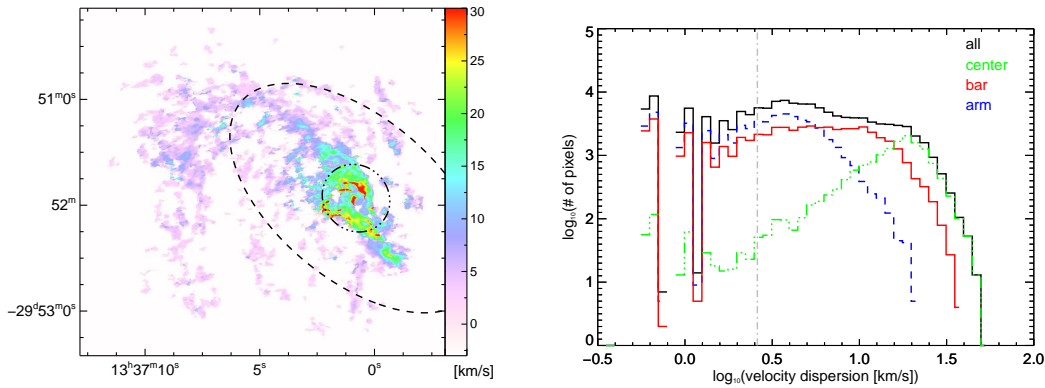


Figure 3. Same as Figure 1, but for σ_V . The vertical gray dot-dashed line is the channel width (2.6 km/s).

the positive feedback effect, in which the swept-out gas forms the next generation stars (e.g. Deharveng et al. 2010). However, this could also be due to the bias that the sources are mostly around the spiral arm where the gas density is generally high. For further discussion, CO data at a higher spatial resolution (< 10 pc considering the size distribution of feedback sources) are essential.

3.2.2. T_{peak} and σ_V PDF

One thing we should note here that PDFs in the simulations are for the gas column density Σ while PDFs from observations are for the I_{CO} . Although X_{CO} is often assumed to be constant within a galaxy, it could vary especially at smaller scales. For example, gas in the feedback area can be heated, which results in brighter CO emission. In addition, the stellar feedback may accelerate gas, which results in larger velocity dispersion. Such positive feedback effects can compensate the negative effect suggested by the simulations.

In Figures 5 and 6, PDFs of T_{peak} and σ_V for the feedback and non-feedback area are presented. While difference in the σ_V PDFs is not clear, the T_{peak} PDF for the feedback area is shallower than that for the non-feedback area. This indicates that an increase of σ_V due to feedback is not evident at the current definition ($r = 2''$), and that gas in the feedback area tends to be warmer and/or a filling factor is larger. The former further suggests that the large σ_V in the bar is not due to stellar feedback. To investigate the cause of difference in T_{peak} PDF profiles, gas temperature and density need to be measured. This requires multi-transition data sets at the same resolution that will be presented in a future paper.

4. MOLECULAR GAS IN M83 BAR

From the PDF analysis described above, we find the I_{CO} tail in the bar of M83. While such a tail has been regarded as a sign of active star formation in MW studies, SFE in the bar of M83 is lower than in the arm. We also find a similar tail for σ_V in the bar and deduce that this large σ_V is a major driver for the I_{CO} tail. Meanwhile, at least at the current spatial scale, stellar feedback does not affect I_{CO} and σ_V PDFs. This suggests that the large σ_V in the bar is not due to feedback. It is rather likely that the large σ_V suppresses star formation in the bar.

There are several other studies suggesting an explanation for low SFE in bars from a dynamical point of view. Based on a large velocity gradient analysis of molecular clouds in Maffei 2, Sorai et al. (2012) suggested that clouds in the bar region are likely unbound and that the X_{CO} factor can be a factor of 2 smaller than that in the arm region. If this is also the case for M83, the Σ PDF

for the bar would not have a clear excess compared to that for the arm, as the current excess in I_{CO} is ~ 0.5 dex, i.e., a factor of ~ 3 . Meidt et al. (2013) presented that a radial area with large streaming motions is associated with low SFEs in a spiral galaxy M51. They interpreted this result that shearing motions can stabilize molecular clouds. These studies support the idea that individual clouds are under a condition which is unlikely to form stars. From a 2D hydrodynamical simulation for M83, Nimori et al. (2013) found that clouds in the bar are more virialized and SFE should be $\sim 60\%$ less in the bar compared to the arm. On the other hand, based on a more recent 3D simulation, Fujimoto et al. (2014a) proposed a scenario that suppressed star formation can be explained by high speed cloud-cloud collisions.

Since these studies focus on molecular clouds, we here briefly summarize cloud properties derived in paper I. Note again that region definitions are not identical. Compared to clouds in the arm, those in the bar are typically larger (radius of 76_{-16}^{+55} pc for the bar and 62_{-14}^{+20} pc for the arm), with higher T_{peak} ($5.2_{-0.9}^{+2.4}$ K for the bar and $3.8_{-1.1}^{+1.0}$ K for the arm), with larger σ_V ($18.7_{-4.5}^{+17.1}$ km/s for the bar and $11.9_{-2.9}^{+3.5}$ km/s for the arm), and with larger virial parameter ($1.6_{-0.5}^{+2.1}$ for the bar and $1.0_{-0.4}^{+0.5}$ for the arm). This result is consistent with the idea that cloud property itself is against star formation. However, there is a possibility that large clouds with large velocity dispersion are a result of cloud-cloud collisions. Furthermore, the differences of the above parameters between the bar and arm are rather small and comparable to their dispersions. For further discussion, again, gas density needs to be derived more accurately without assuming a constant conversion factor.

5. SUMMARY

Based on ALMA and NRO45m observations toward M83 in CO(1–0) at 40 pc scale, we create PDFs of I_{CO} , T_{peak} , and σ_V . This work is complementary to paper I, which identifies molecular clouds based on the same data set and investigates their properties.

We first investigate PDF profiles according to the galactic structure, i.e. center, bar, and arm. The I_{CO} PDF for the bar shows an excess or tail at the bright end ($I_{\text{CO}} \gtrsim 100$ K km/s) compared to that for the arm. From PDF studies of MW molecular clouds, such a bright-end tail is often interpreted as a sign of self-gravity and/or star formation. However, SFE in M83 bar is lower than in arms. The σ_V PDF for the bar also shows an excess at $\sigma_V \gtrsim 10$ km/s, suggesting that this large velocity dispersion in the bar is a major cause of the I_{CO} tail and low SFE. This result indicates that at

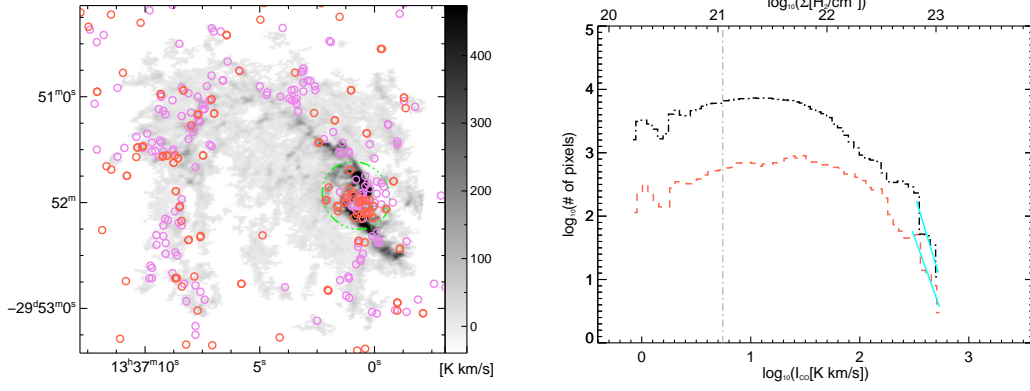


Figure 4. *Left:* Circles indicate the positions of young stellar clusters or HII regions (purple) and SNRs (red) with a radius of $2''$. The background image is the I_{CO} map (same as Figure 1, but in a different color). *Right:* PDFs for feedback (red dashed) and non-feedback (black dot-dashed) area. The center region is excluded. Cyan solid lines indicate the linear fit results at the bright end.

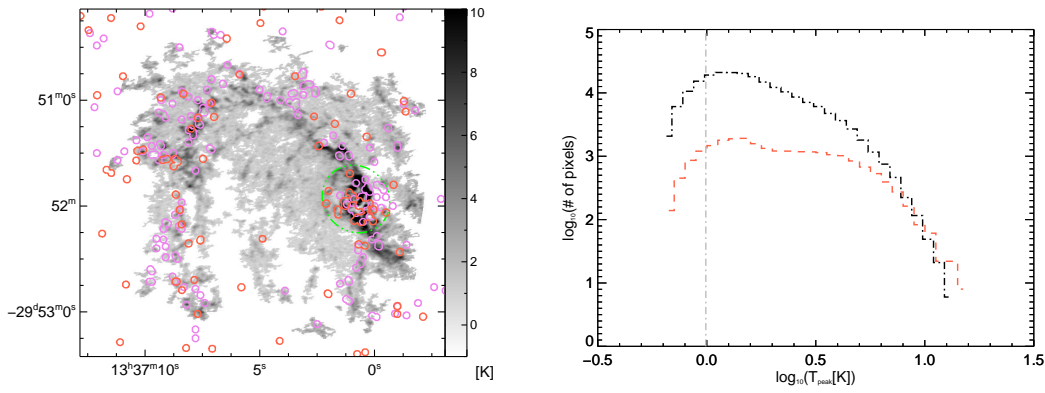


Figure 5. Same as Figure 4, but for T_{peak} .

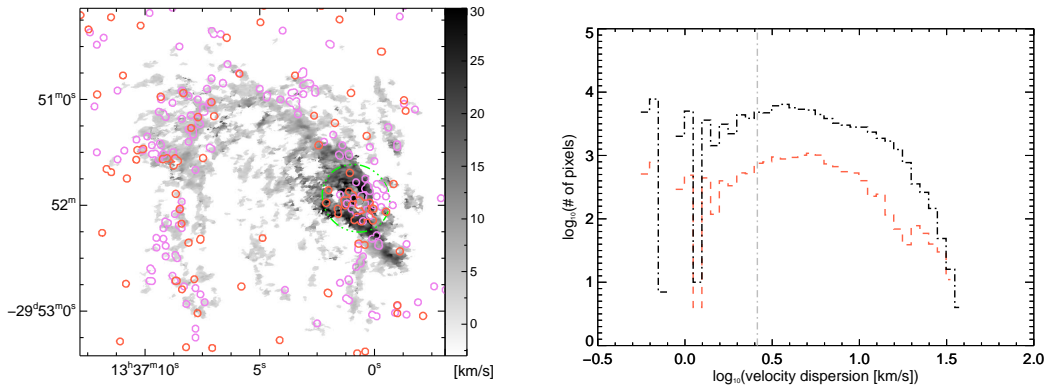


Figure 6. Same as Figure 4, but for σ_V .

least at 40 pc scale the I_{CO} tail is not always a sign of active star formation.

We also investigate if stellar feedback affects PDF profiles. A feedback area and non-feedback area are defined according to catalogs of HII regions, young star clusters, and SNRs. The radius of the feedback area is set to be $2''$ (~ 40 pc). While the T_{peak} PDF is shallower for the feedback area, σ_V and I_{CO} PDFs do not differ significantly between the two areas. We thus conclude that at least at 40 pc scale the feedback effect does not explain the different PDFs between bar and arm regions.

These results suggest that the large-scale disk structures affect PDFs of σ_V and thus of I_{CO} while the small-scale feedback affects the T_{peak} PDF.

We appreciate careful reading and suggestions by a referee that have improved our manuscript.

This paper makes use of the following ALMA data: ADS/JAO.ALMA#2011.0.00772.S. ALMA is a partnership of ESO (representing its member states), NSF (USA) and NINS (Japan), together with NRC (Canada), NSC and ASIAA (Taiwan), and KASI (Republic of Korea), in cooperation with the Republic of Chile. The Joint ALMA Observatory is operated by ESO, AUI/NRAO and NAOJ. The Nobeyama 45-m radio telescope is operated by Nobeyama Radio Observatory, a branch of National Astronomical Observatory of Japan.

Facilities: ALMA, Nobeyama 45m Telescope

APPENDIX

As mentioned in §3, σ_V (moment 2 of the CO cube) is not corrected for the galactic rotation and beam smearing. In order to estimate their effect on σ_V PDF profiles, we have generated a model cube assuming that the disk is super-thin and uniform. The model rotation curve in Figure 21 of H14 and the disk orientation parameters in their Table 1 have been adopted. The model cube has been smoothed with the synthesized beam mentioned in §2.3, and then converted to a moment 2 map. We have found that the model velocity dispersion is at most 4.3 km/s and generally decreases with radius. As a result, differences between observed σ_V and model-subtracted σ_V are visible only when σ_V is smaller than the channel width (2.6 km/s). Since we mostly focus on high-end ($\sigma_V \gtrsim 10$ km/s) profiles of σ_V PDFs for the bar and arm regions, the effect of the galactic rotation and beam smearing does not change our conclusions. Even for the center region, the effect only appears on the low-end profile.

REFERENCES

- Berkhuijsen, E. M., & Fletcher, A. 2015, MNRAS, 448, 2469
- Blair, W. P., Winkler, P. F., & Long, K. S. 2012, ApJS, 203, 8
- Blair, W. P., Chandar, R., Dopita, M. A., et al. 2014, ApJ, 788, 55
- Bolatto, A. D., Wolfire, M., & Leroy, A. K. 2013, ARA&A, 51, 207
- Brunt, C. M. 2015, MNRAS, 449, 4465
- Colombo, D., Hughes, A., Schinnerer, E., et al. 2014, ApJ, 784, 3
- Comte, G. 1981, A&AS, 44, 441
- Dame, T. M., Hartmann, D., & Thaddeus, P. 2001, ApJ, 547, 792
- de Vaucouleurs, G., de Vaucouleurs, A., Corwin, Jr., H. G., et al. 1991, Third Reference Catalogue of Bright Galaxies. Volume I: Explanations and references. Volume II: Data for galaxies between 0^h and 12^h . Volume III: Data for galaxies between 12^h and 24^h .
- Deharveng, L., Schuller, F., Anderson, L. D., et al. 2010, A&A, 523, A6
- Dobbs, C. L., & Pringle, J. E. 2013, MNRAS, 432, 653
- Dopita, M. A., Blair, W. P., Long, K. S., et al. 2010, ApJ, 710, 964
- Druard, C., Braine, J., Schuster, K. F., et al. 2014, A&A, 567, A118
- Egusa, F., Koda, J., & Scoville, N. 2011, ApJ, 726, 85
- Elmegreen, B. G. 2011, ApJ, 731, 61
- Fujimoto, Y., Tasker, E. J., & Habe, A. 2014a, MNRAS, 445, L65
- Fujimoto, Y., Tasker, E. J., Wakayama, M., & Habe, A. 2014b, MNRAS, 439, 936
- Girichidis, P., Konstandin, L., Whitworth, A. P., & Klessen, R. S. 2014, ApJ, 781, 91
- Hirota, A., Kuno, N., Sato, N., et al. 2011, ApJ, 737, 40
- Hirota, A., Kuno, N., Baba, J., et al. 2014, PASJ, 66, 46
- Hopkins, P. F., Quataert, E., & Murray, N. 2012, MNRAS, 421, 3488

- Hughes, A., Meidt, S. E., Schinnerer, E., et al. 2013, *ApJ*, 779, 44
- Kainulainen, J., Beuther, H., Henning, T., & Plume, R. 2009, *A&A*, 508, L35
- Knapen, J. H., Sharp, R. G., Ryder, S. D., et al. 2010, *MNRAS*, 408, 797
- Koda, J., Scoville, N., Sawada, T., et al. 2009, *ApJL*, 700, L132
- Koda, J., Scoville, N., Hasegawa, T., et al. 2012, *ApJ*, 761, 41
- Kritsuk, A. G., Norman, M. L., & Wagner, R. 2011, *ApJL*, 727, L20
- Meidt, S. E., Schinnerer, E., García-Burillo, S., et al. 2013, *ApJ*, 779, 45
- Momose, R., Okumura, S. K., Koda, J., & Sawada, T. 2010, *ApJ*, 721, 383
- Nguyen, N. K., Pettitt, A. R., Tasker, E. J., & Okamoto, T. 2017, *ArXiv e-prints*, arXiv:1712.00957
- Nimori, M., Habe, A., Sorai, K., et al. 2013, *MNRAS*, 429, 2175
- Nordlund, Å. K., & Padoan, P. 1999, in *Interstellar Turbulence*, ed. J. Franco & A. Carraminana, 218
- Ossenkopf-Okada, V., Csengeri, T., Schneider, N., Federrath, C., & Klessen, R. S. 2016, *A&A*, 590, A104
- Pan, H.-A., & Kuno, N. 2017, *ApJ*, 839, 133
- Rathborne, J. M., Longmore, S. N., Jackson, J. M., et al. 2014, *ApJL*, 795, L25
- Sawada, T., Hasegawa, T., & Koda, J. 2012a, *ApJL*, 759, L26
- Sawada, T., Hasegawa, T., Sugimoto, M., Koda, J., & Handa, T. 2012b, *ApJ*, 752, 118
- Sheth, K., Vogel, S. N., Regan, M. W., et al. 2002, *AJ*, 124, 2581
- Sorai, K., Kuno, N., Nishiyama, K., et al. 2012, *PASJ*, 64, 51
- Thim, F., Tammann, G. A., Saha, A., et al. 2003, *ApJ*, 590, 256
- Tosaki, T., Kohno, K., Harada, N., et al. 2017, *PASJ*, arXiv:1612.00948
- Wada, K., & Norman, C. A. 2007, *ApJ*, 660, 276
- Whitmore, B. C., Chandar, R., Kim, H., et al. 2011, *ApJ*, 729, 78
- Wofford, A., Leitherer, C., & Chandar, R. 2011, *ApJ*, 727, 100
- Young, J. S., & Scoville, N. Z. 1991, *ARA&A*, 29, 581